



Short communication

Free-standing Pt@RuO₂·xH₂O nanorod arrays on Si wafers as electrodes for methanol electro-oxidation



Guangyu Zhao ^a, Li Zhang ^a, Kening Sun ^{a,*}, Hulin Li ^b

^a Academy of Fundamental and Interdisciplinary Sciences, Harbin Institute of Technology, Harbin, Heilongjiang 150080, PR China

^b College of Chemistry and Chemical Engineering, Lanzhou University, Lanzhou 730000, PR China

HIGHLIGHTS

- Pt@RuO₂·xH₂O nanorod arrays free-standing on Si wafers.
- Uniform distribution of Pt nanoparticles coated on RuO₂·xH₂O nanorods.
- A practical route for fabricating micro fuel cell electrodes.

ARTICLE INFO

Article history:

Received 15 May 2013

Received in revised form

2 July 2013

Accepted 11 July 2013

Available online 20 July 2013

Keywords:

Anodic aluminum oxide template

Silicon wafer

Nanorod array

Electro-catalysis

Poisoning rate

ABSTRACT

RuO₂·xH₂O nanorod arrays free-standing on Si wafers are prepared by an anodic aluminum oxide template assistant method. Pt nanograins in the size of 3–5 nm are deposited on the RuO₂·xH₂O nanorod arrays uniformly by a cool sputtering approach. Electrochemical measurements indicate that, the Pt@RuO₂·xH₂O nanorod arrays have larger electrochemical active areas (EAAs) and better poisoning resistant ability for methanol electro-oxidation, compared with Pt nanograins that deposited on Ti wafers directly (named Pt/Ti). The EAAs of Pt@RuO₂·xH₂O and Pt/Ti electrodes are 40.6 and 31.1 m² g⁻¹, respectively. The poisoning rate of Pt@RuO₂·xH₂O arrays is 8.9 × 10⁻⁴ per second, much smaller than that of Pt/Ti electrodes (3.4 × 10⁻³ per second).

© 2013 Elsevier B.V. All rights reserved.

1. Introduction

Micro-electromechanical systems (MEMSs) on Si substrates arising from the integrated circuit technology have established high volume commercial markets for accelerometers and pressure sensors in the automotive industry successfully. Micro fuel cells are promising high energy density power sources for MEMSs [1]. When integrating micro fuel cells as on-chip devices into MEMSs used for sensors/actuators and other micro-devices, the processes of manufacturing electro-catalysis electrodes and the remaining fuel cell system must be post-CMOS (Complementary Metal Oxide Semiconductor) compatible [2,3]. However,

it is difficult to manufacture conventional carbon-supported catalyst membranes by MEMS fabrication methods, due to the instability of carbon in the CMOS process. Therefore, a Si-based carbon-free electrode becomes necessary for micro fuel cells. Several kinds of catalyst layers deposited on Si wafers by electrodeposition [2,3], sputtering [4,5] and evaporation [6–8] have been reported. However, the researchers used self-supporting structures for the catalysts these studies, instead of proposing a new supporting material for catalyst layers. The self-supporting structures result in a low utilization of the catalysts, because of the catalyst grains accumulating on the Si substrates. These structures also fail to create fluent ion transmission channels, which are beneficial to shorten the diffusion distance in electro-catalysis processes [9,10].

RuO₂·xH₂O is a good candidate for substituting carbon as the supporting material of fuel cell catalysts, since the high electron and proton conductivity [11,12], as well as the assisting oxidation of CO or CHO species by adsorption of oxygen-containing species

* Corresponding author. Tel./fax: +86 451 86412153.

E-mail address: keningsun@yahoo.com.cn (K. Sun).

close to the poisoned Pt catalyst sites [13]. Anodic aluminum oxide (AAO) template assistant method is very helpful for preparing array structures with uniform unhindered channels. The electrodes prepared with this method exhibit prominent performances, when used as electrochemical energy storage and conversion devices [10,14]. Herein, AAO films on Si wafers are fabricated by an anodic oxidation, and used for depositing free-standing $\text{RuO}_2\text{-xH}_2\text{O}$ nanorod arrays. A layer of Pt nanograins is deposited on the arrays by a cool sputtering approach. The free-standing $\text{Pt@RuO}_2\text{-xH}_2\text{O}$ nanorod arrays have a large active area and prominent resistance ability to carbon oxide species poisoning.

2. Experimental

A highly pure Al film (99.99%, $\sim 1.0\ \mu\text{m}$) and a Ti ($\sim 10\ \text{nm}$) layer were deposited on the p-type Si substrate by thermally evaporated deposition to form Al/Ti/Si wafers ($1.0\ \text{cm} \times 1.0\ \text{cm}$). An anodic oxidation was carried out in 0.3 M oxalic acid solution at 40 V and room temperature for 10 min. The resulting alumina film was etched away in the solution of 0.4 M H_3PO_4 + 0.2 M $\text{H}_2\text{Cr}_2\text{O}_4$ at $50\ ^\circ\text{C}$ for 0.5 h. The remaining Al was re-anodized under the same conditions until the Al film was oxidized completely. The electrolyte for electrodeposition consisted of 10 mM RuCl_3 and 1.2 mM HCl. The electrodeposition was carried out using a cyclic voltammogram (CV) method in a potential window of $-0.8\text{--}2.0\ \text{V}$ (vs. SCE) with a scan rate of $50\ \text{mV s}^{-1}$ on a CHI 660 electrochemical analyzer. The as-prepared samples were immersed in 0.01 M NaOH for 1 h to remove the AAO films. Pt nanograins were deposited on $\text{RuO}_2\text{-xH}_2\text{O}$ nanorod arrays by a Leica EM SC050 cool sputtering device at a current of 40 mA for 40 s. For comparison, Pt nanograins deposited on Ti wafers (Pt/Ti) were also prepared with the same conditions.

A conventional cell with a three-electrode configuration was used in this work. The $\text{Pt@RuO}_2\text{-xH}_2\text{O}$ nanorod arrays and Pt/Ti were employed as the working electrodes, a $1.0\ \text{cm} \times 1.0\ \text{cm}$ platinum plate as counter electrode and a SCE as the reference electrode. Electrochemical measurements were performed at room temperature with the CHI 660 electrochemical analyzer. Scanning electron microscope (SEM) images were obtained on a Hitachi SU-8100. The X-ray diffraction (XRD) patterns were obtained on a PANalytical X'pert PRO X-ray diffractometer with $\text{Cu K}\alpha$ radiation ($\lambda = 1.5418\ \text{\AA}$). Transmission electron microscope (TEM) images and energy dispersive X-ray spectra (EDS) patterns were obtained on a FEI Tecnai G². X-ray photoelectron spectra (XPS) were tested with a $\text{K}\alpha$ electron spectrometer from ThermoFisher Scientific Company

using $\text{Al K}\alpha$ (1486.6 eV) radiation. The base pressure was about $1 \times 10^{-8}\ \text{mbar}$. The binding energies were referenced to the C1s line at 284.8 eV from adventitious carbon.

3. Results and discussion

The SEM images of AAOs' surface are shown in Fig. 1. The nanoholes are not very regular, compared with the AAO templates obtained on the traditional thick Al foils, because of the ultrathin Al films used in our work. It is known that the longer anodic time, the more regular nanoholes can be obtained [15]. However, these holes standing on Ti current collector vertically are competent for growing free-standing nanorod arrays. CV was employed to deposit $\text{RuO}_2\text{-xH}_2\text{O}$ nanorods. In the CV process, the Ru^{3+} ions were reduced to metal Ru in cathodic sweeping, then the Ru metal was oxidized to $\text{RuO}_2\text{-xH}_2\text{O}$ in the subsequent anodic sweeping [16]. The generated $\text{RuO}_2\text{-xH}_2\text{O}$ could not be reduced in the following cathodic process. Therefore, the sequential sweeping led the nanorods growing continuously [17]. The $\text{Pt@RuO}_2\text{-xH}_2\text{O}$ nanorod arrays were obtained by dissolving the AAO templates and sputtering Pt nanograins.

The XRD results of Pt/Ti and $\text{Pt@RuO}_2\text{-xH}_2\text{O}$ electrodes have been presented in Fig. S1. The peaks in the pattern of Pt/Ti can be ascribed to the Ti wafer substrate (JCPDS: 65-6231). The absence of Pt diffraction peaks can be attributed to the ultra-small amount of Pt nanoparticles deposited on the substrates by the cool sputtering approach. For the same reason, the Pt diffraction peaks do not appear in the pattern of $\text{Pt@RuO}_2\text{-xH}_2\text{O}$ electrode either. Conversely, the peaks of Ti (JCPDS: 65-5970) and RuO_2 (JCPDS: 40-1290) can be detected clearly. Additionally, the different crystal forms of Ti in the two electrodes may arise from the different preparation methods of Ti substrates.

XPS measurement was used for investigating the Pt catalyst deposited by the cool sputtering approach. The peaks of Pt can be observed clearly from the XPS survey pattern of Pt/Ti electrodes in Fig. S2. The XPS patterns of $\text{Pt@RuO}_2\text{-xH}_2\text{O}$ arrays are shown in Fig. 2, in which, the peaks of Pt 4f, C 1s, Pt 4d, Pt 4p, Ti 2p, and O 1s present in the survey pattern. In Pt 4f of Fig. 2(b), the XPS spectra are characterized by a doublet containing a binding energy of 71.05 eV (Pt 4f7/2) and 74.4 eV (Pt 4f5/2). The two peaks have a binding energy difference of 3.35 eV and a peak area ratio of 4:3, which corresponds to the characteristics of Pt (0). The Pt 4f spectrum can be deconvoluted into two species with binding energies of 71.05–74.4 and 72–76.2 eV, corresponding to Pt (0) and Pt (II), respectively [18]. On the basis of the areas of Pt 4f7/2 and Pt 4f5/2,

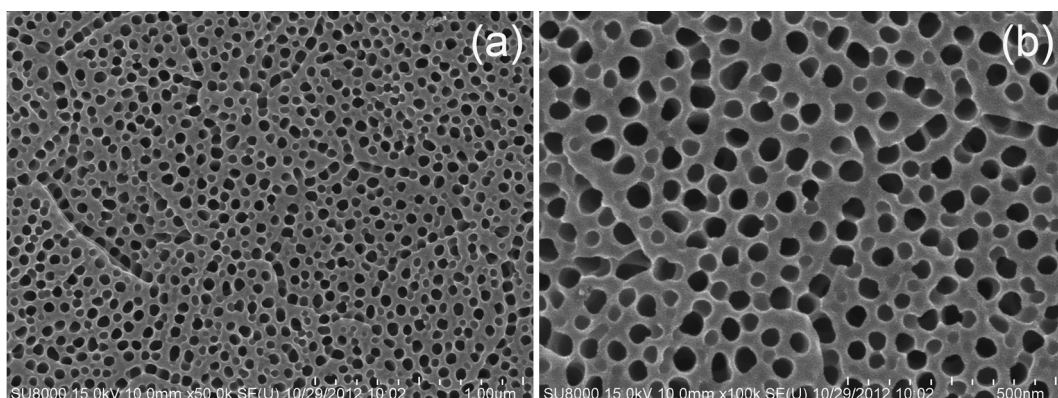


Fig. 1. SEM images of AAO templates on Si wafers.

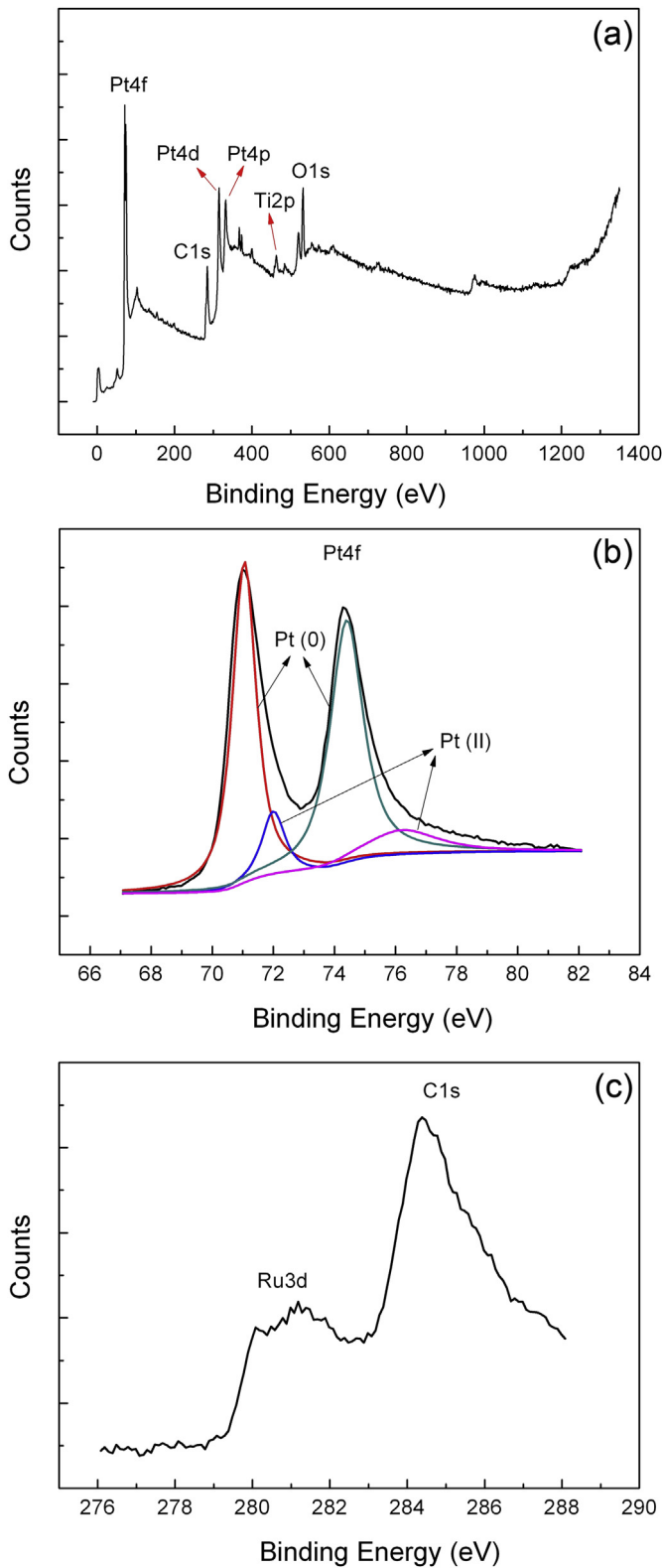


Fig. 2. XPS results of $\text{Pt}@\text{RuO}_2\text{-xH}_2\text{O}$ nanorods: survey (a), high resolution spectra of Pt 4f (b) and Ru 3d (c).

the relative intensity of Pt (0) and Pt (II) was calculated to be 83% and 17%, respectively. This indicates that the Pt in $\text{Pt}@\text{RuO}_2\text{-xH}_2\text{O}$ nanorod arrays would be Pt metal primarily, which is significant to electro-catalysis reactions [18]. The high resolution spectrum of Ru

3d containing a binding energy of 281 eV in Fig. 2(c) reveals the existence of RuO_2 .

The morphologies and EDS pattern of $\text{Pt}@\text{RuO}_2\text{-xH}_2\text{O}$ nanorods are shown in Fig. 3. From Fig. 3(a) and (b), it is clearly seen that the nanorods are free-standing on the substrates uniformly. This “nano-brush” architecture results in a larger active area for electro-catalysis than the Pt/Ti electrodes, which can be verified by the electrochemical measurements. In the high magnification image of Fig. 3(c), we can see that, the diameter of the nanorods is about 40 nm, identical with the nanoholes of AAO templates. Small Pt nanograins distribute homogeneously on the nanorods, suggesting the cool sputtering approach is effective and controllable to deposit nanograins. The nanorods were scraped from the Si wafers for the EDS and TEM measurements. The EDS in Fig. 3(d) demonstrates the existence of Pt, Ru and O elements, which are all from the $\text{Pt}@\text{RuO}_2\text{-xH}_2\text{O}$ nanorods. The EDS mapping images of a $\text{Pt}@\text{RuO}_2\text{-xH}_2\text{O}$ nanorod have been presented in Fig. S3. The maps of Pt (Pt-L and Pt-M) and Ru (Ru-K and Ru-L) elements exhibit that, a layer of Pt is coated on the $\text{RuO}_2\text{-xH}_2\text{O}$ uniformly. Furthermore, the edge of the nanorod has a higher Pt content than the other area, showing the homogeneous distribution of Pt nanoparticles on the nanorod. Additionally, the EDS quantification results for this typical nanorod indicate that, the loading of Pt on $\text{RuO}_2\text{-xH}_2\text{O}$ support material is 16.92% of a nanorod (Weight). In the TEM image of Fig. 3(e), the length of the nanorods is about 300 nm, and a layer of Pt nanograins are coated on the nanorods. Fig. 3(f) indicates that, the Pt nanograins are 3–5 nm, the optimal size for methanol electro-catalysis [19].

CV curves of Pt/Ti and $\text{Pt}@\text{RuO}_2\text{-xH}_2\text{O}$ electrodes at room temperature obtained in 0.5 M H_2SO_4 electrolyte are shown in Fig. 4(a) and (b). The hydrogen sorption/desorption peaks of the CV curves are not well-defined. In acid solution, well-defined peaks ascribed to the hydrogen sorption/desorption on the crystal faces of Pt(110), Pt(100) and Pt(111) should be detected from the CV of Pt metal. However, the well-defined peaks usually arise on the bigger Pt particles, which have these crystal faces clearly. Only one sharp hydrogen sorption/desorption peak can be detected commonly, when the Pt nanoparticles are ultra-small (for instance, several nanometers), because of the high content of the low coordination number Pt atoms. These low coordination number Pt atoms cause the hydrogen sorption/desorption on Pt nanoparticles to exhibit two sharp peaks in the low potential region of CV curves [20]. The coulombic charge for hydrogen sorption/desorption (Q_H) was used for estimating the electrochemical active areas (EAAs) of the electrodes [21]:

$$\text{EAA} = \frac{Q_H}{[\text{Pt}] \times 0.21}, \quad (1)$$

$$Q_H = \frac{Q' + Q''}{2}, \quad (2)$$

where $[\text{Pt}]$ represents the Pt loading (mg cm^{-2}) in an electrode, Q_H represents the charge for hydrogen sorption/desorption (mC cm^{-2}) and 0.21 represents the charge required to oxidize a monolayer of H_2 on bright Pt [20]. Q_H can be calculated from the average value of hydrogen sorption (Q') and desorption (Q'') charge, as demonstrated in Fig. 4(a) and (b). The EAAs of Pt/Ti and $\text{Pt}@\text{RuO}_2\text{-xH}_2\text{O}$ electrodes calculated from the formulas are 31.1 and $40.6 \text{ m}^2 \text{ g}^{-1}$, respectively.

The CVs for methanol oxidation on Pt/Ti and $\text{Pt}@\text{RuO}_2\text{-xH}_2\text{O}$ electrodes' surface in 0.5 M H_2SO_4 containing 0.5 M methanol solution are shown in Fig. 4(c) and (d). There are two methanol oxidation peaks on Pt/Ti electrodes in the anodic/cathodic sweeps

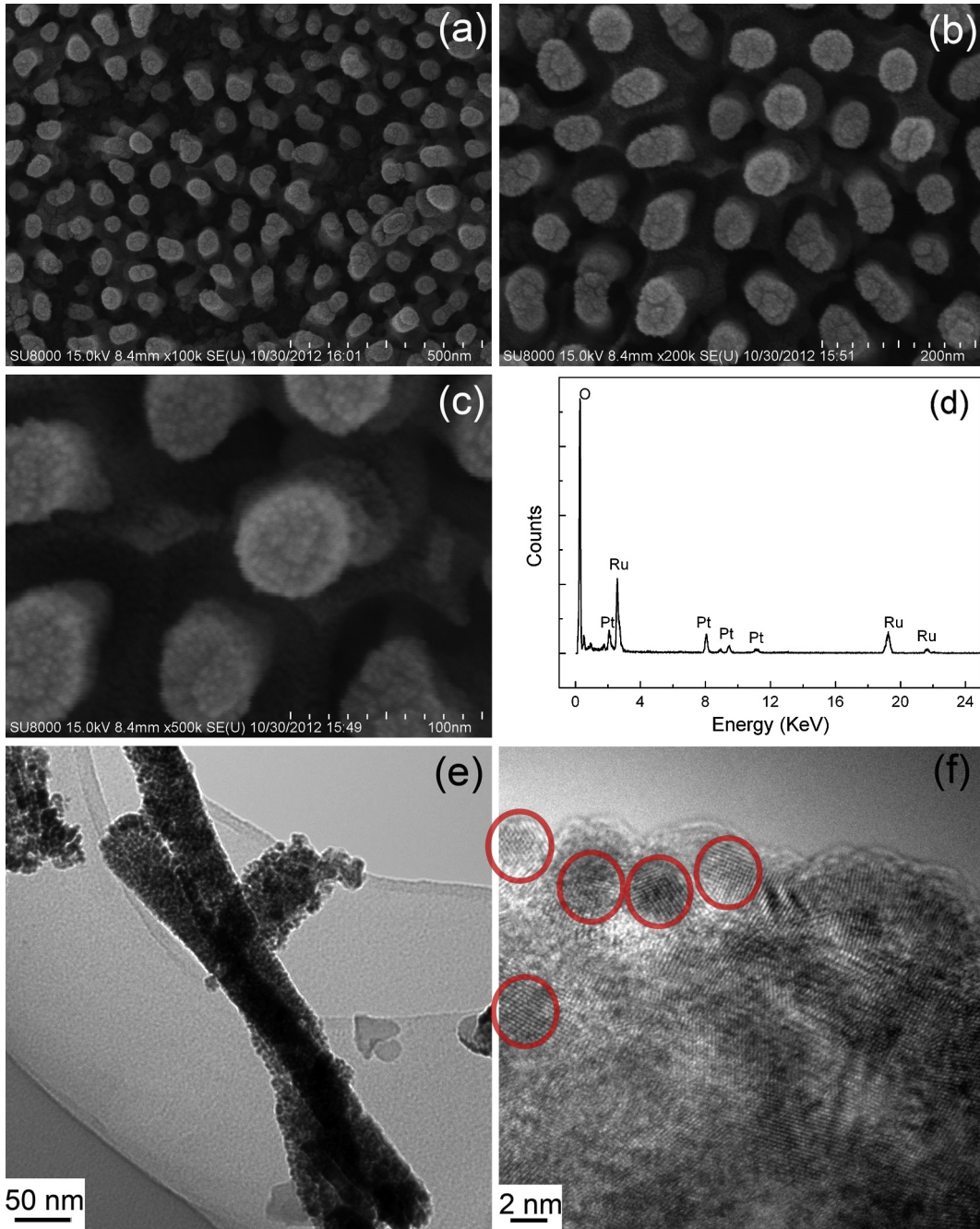


Fig. 3. SEM images (a, b, c), EDS (d) pattern of Pt@RuO₂·xH₂O arrays, and TEM images (e, f) of Pt@RuO₂·xH₂O nanorods scraped from the substrates.

at 0.65 and 0.5 V, respectively. Nevertheless, the peaks are very weak, compared with those on the Pt@RuO₂·xH₂O nanorod electrodes. Characteristic doublet peaks for methanol electro-oxidation can be detected for that of Pt@RuO₂·xH₂O nanorod array electrodes, consistent with the peak shapes in other work [22]. We suggest the weak peaks in CVs of Pt/Ti electrode owing to the poor distribution of Pt nanoparticles on Ti wafer, because of the low surface area of flat Ti wafers compared with the nanorod array electrodes. Another improvement of Pt@RuO₂·xH₂O electrodes is the better resistance to poisoning, which can be evaluated by the poisoning rate δ , calculated from the chronoamperometry curves in Fig. 4(e) and (f) [23,24]:

$$\delta = \frac{100}{I_0} \times \left(\frac{dI}{dt} \right)_{t>500 \text{ s}}, \quad (3)$$

where $(dI/dt)_{t>500 \text{ s}}$ is the slope of the linear portion of the current decay and I_0 is the current at the start of polarization back extrapolated from the linear current decay. The calculated δ value of Pt/Ti and Pt@RuO₂·xH₂O electrodes are 3.4×10^{-3} and 8.9×10^{-4} (% per second), respectively. Ruthenium oxide is acknowledged as a prominent accelerating reagent for oxidizing the (CO)_{ads} on Pt catalyst, which is the main poisoning species. Therefore, the Pt@RuO₂·xH₂O electrodes exhibit a smaller poisoning rate after a long time polarization process.

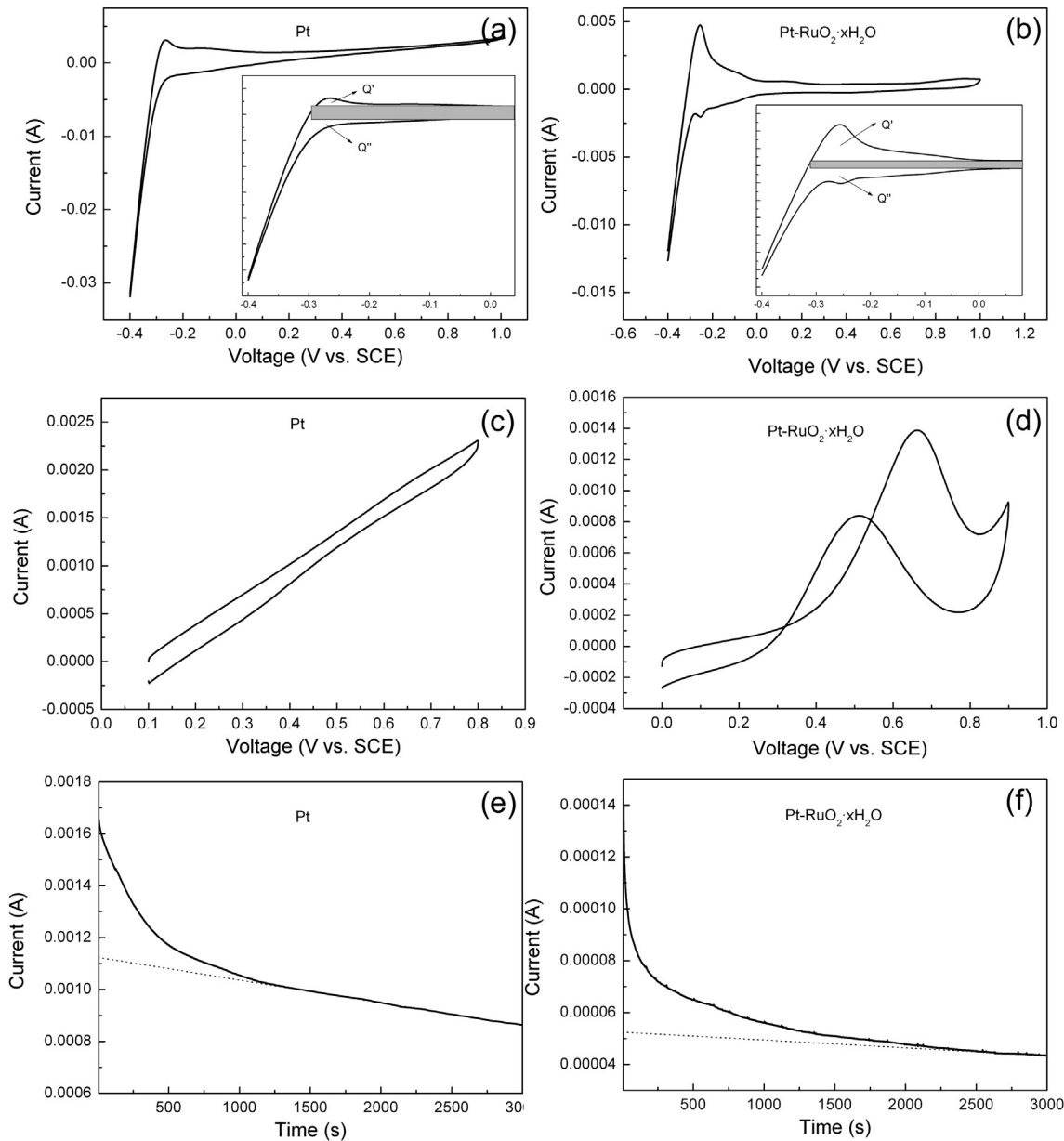


Fig. 4. CV curves of Pt/Ti (a) and Pt@RuO₂·xH₂O (b) electrodes in 0.5 M H₂SO₄, insets are the amplificatory curves of hydrogen adsorption/desorption; CV curves of Pt/Ti (c) and Pt@RuO₂·xH₂O (d) electrodes in 0.5 M H₂SO₄ + 0.5 M CH₃OH electrolyte at a scan rate of 50 mV s⁻¹; and the chronoamperometry curves of Pt/Ti (e) and Pt@RuO₂·xH₂O (f) electrodes in the electrolyte of 0.5 M H₂SO₄ + 0.5 M CH₃OH.

4. Conclusions

Pt nanograins coated free-standing RuO₂·xH₂O nanorod arrays on Si wafers were prepared by an AAO template assistant method. The CV results indicate that, the Pt@RuO₂·xH₂O electrodes have a larger active area than Pt nanograins deposited on Ti wafers directly, owing to the array architecture. Another improvement of array electrodes is the prominent poisoning resistant ability, because of the synergistic effect of Pt with RuO₂·xH₂O. The electrodes proposed in this study have free-standing array architectures, which can improve the utilization of catalysts. The RuO₂·xH₂O supporting material endows the array electrodes a good resistant ability to poisoning. This strategy of preparing array electrodes will be a practical post-CMOS compatible route for fabricating micro MEMS-base fuel cell electrodes.

Acknowledgments

This work was supported by the National Science Foundation of China (NSFC) (no. 20903031 and no. 21203044).

Appendix A. Supplementary data

Supplementary data related to this article can be found at <http://dx.doi.org/10.1016/j.jpowsour.2013.07.053>.

References

- [1] J.W. Long, B. Dunn, D.R. Rolison, H.S. White, *Chem. Rev.* 104 (2004) 4463–4492.
- [2] C. Feng, Z. Xiao, C.H. Chan Philip, I.-M. Hsing, *Electrochim. Commun.* 8 (2006) 1235–1238.
- [3] J. Yeom, R.S. Jayashree, C. Rastogi, M.A. Shannon, P.J.A. Kenis, *J. Power Sources* 160 (2006) 1058–1064.

[4] K. Shah, W.C. Shin, R.S. Besse, *J. Power Sources* 123 (2003) 172–181.

[5] K. Shah, W.C. Shin, R.S. Besser, *Sens. Actuators B* 97 (2004) 157–167.

[6] Y. Yamazaki, *Electrochim. Acta* 50 (2004) 663–666.

[7] J. Li, C. Moore, P.A. Kohl, *J. Power Sources* 138 (2004) 211–215.

[8] J. Yeom, G.Z. Mozsgai, B.R. Flachsbart, E.R. Choban, A. Asthana, M.A. Shannon, P.J.A. Kenis, *Sens. Actuators B* 107 (2005) 882–891.

[9] F. Cheng, Z. Tao, J. Liang, J. Chen, *Chem. Mater.* 20 (2008) 667–681.

[10] C. Xu, H. Wang, P.K. Shen, S.P. Jiang, *Adv. Mater.* 19 (2007) 4256–4259.

[11] D.R. Rolison, P.L. Hagans, K.E. Swider, J.W. Long, *Langmuir* 15 (1999) 774–779.

[12] G. Mangiapia, D. Berti, P. Baglioni, J. Teixeira, L. Paduano, *J. Phys. Chem. B* 108 (2004) 9772–9779.

[13] L. Cao, F. Scheiba, C. Roth, F. Schweiger, C. Cremer, U. Stimming, H. Fuess, L. Chen, W. Zhu, X. Qiu, *Angew. Chem. Int. Ed.* 45 (2006) 5315–5319.

[14] S.S. Mahshid, S. Mahshid, A. Dolati, M. Ghorbani, L. Yang, S. Luo, Q. Cai, *Electrochim. Acta* 58 (2011) 551–555.

[15] W. Lee, R. Ji, U. Gösele, K. Nielsch, *Nat. Mater.* 5 (2006) 741–747.

[16] C.C. Hu, K.H. Chang, M.C. Lin, Y.T. Wu, *Nano Lett.* 6 (2006) 2690–2695.

[17] C.C. Hu, Y.H. Huang, *J. Electrochem. Soc.* 146 (1999) 2465–2471.

[18] Z.Q. Tian, S.P. Jiang, Y.M. Liang, P.K. Shen, *J. Phys. Chem. B* 110 (2006) 5343–5350.

[19] K. Bergamaski, A.L.N. Pinheiro, E. Teixeira-Neto, F.C. Nart, *J. Phys. Chem. B* 110 (2006) 19271–19279.

[20] W. Vielstich, A. Lamm, H.A. Gasteiger, *Handbook of Fuel Cell: Fundamentals Technology and Applications*, vol. 2, 2003, pp. 153–155.

[21] A. Pozio, M. Francesco, A. Cemmi, F. Cardellini, L. Giorgi, *J. Power Sources* 105 (2002) 13–19.

[22] K. Yahikozawa, Y. Fujii, Y. Mitsuda, K. Nishimura, Y. Takasu, *Electrochim. Acta* 36 (1991) 973–979.

[23] J. Jiang, A. Kucernak, *J. Electroanal. Chem.* 543 (2003) 187–199.

[24] J.W. Guo, T.S. Zhao, J. Prabhuram, R. Chen, C.W. Wong, *J. Power Sources* 156 (2006) 345–354.